

Clustering of Star-forming Galaxies Near a Radio Galaxy at

$$z = 5.2^1$$

Roderik A. Overzier², G.K. Miley², R.J. Bouwens³, N.J.G. Cross⁴, A.W. Zirm², N. Benítez⁵, J.P. Blakeslee⁶, M. Clampin⁷, R. Demarco⁶, H.C. Ford⁶, G.F. Hartig⁸, G.D. Illingworth³, A.R. Martel⁶, H.J.A. Röttgering², B. Venemans², D.R. Ardila⁶, F. Bartko⁹, L.D. Bradley⁶, T.J. Broadhurst¹⁰, D. Coe⁶, P.D. Feldman⁶, M. Franx², D.A. Golimowski⁶, T. Goto⁶, C. Gronwall¹¹, B. Holden³, N. Homeier⁶, L. Infante¹², R.A. Kimble⁷, J.E. Krist¹³, S. Mei⁶, F. Menanteau⁶, G.R. Meurer⁶, V. Motta^{6,12}, M. Postman⁸, P. Rosati¹⁴, M. Sirianni⁶, W.B. Sparks⁸, H.D. Tran¹⁵, Z.I. Tsvetanov⁶, R.L. White⁸ & W. Zheng⁶

overzier@strw.leidenuniv.nl

ABSTRACT

¹Based on observations made with the NASA/ESA Hubble Space Telescope, which is operated by the Association of Universities for Research in Astronomy, Inc., under NASA contract NAS 5-26555. These observations are associated with program # 9291

²Leiden Observatory, Postbus 9513, 2300 RA Leiden, Netherlands.

³UCO/Lick Observatory, University of California, Santa Cruz, CA 95064.

⁴Royal Observatory Edinburgh, Blackford Hill, Edinburgh, EH9 3HJ, UK

⁵Inst. Astrofísica de Andalucía (CSIC), Camino Bajo de Huétor, 24, Granada 18008, Spain

⁶Department of Physics and Astronomy, The Johns Hopkins University, 3400 North Charles Street, Baltimore, MD 21218.

⁷NASA Goddard Space Flight Center, Code 681, Greenbelt, MD 20771.

⁸STScI, 3700 San Martin Drive, Baltimore, MD 21218.

⁹Bartko Science & Technology, 14520 Akron Street, Brighton, CO 80602.

¹⁰Racah Institute of Physics, The Hebrew University, Jerusalem, Israel 91904.

¹¹Department of Astronomy and Astrophysics, The Pennsylvania State University, 525 Davey Lab, University Park, PA 16802.

¹²Departamento de Astronomía y Astrofísica, Pontificia Universidad Católica de Chile, Casilla 306, Santiago 22, Chile.

¹³Jet Propulsion Laboratory, M/S 183-900, 4800 Oak Grove Drive, Pasadena, CA 91109

¹⁴European Southern Observatory, Karl-Schwarzschild-Strasse 2, D-85748 Garching, Germany.

¹⁵W. M. Keck Observatory, 65-1120 Mamalahoa Hwy., Kamuela, HI 96743

We present HST/ACS observations of the most distant radio galaxy known, TN J0924–2201 at $z = 5.2$. This radio galaxy has 6 spectroscopically confirmed Ly α emitting companion galaxies, and appears to lie within an overdense region. The radio galaxy is marginally resolved in i_{775} and z_{850} showing continuum emission aligned with the radio axis, similar to what is observed for lower redshift radio galaxies. Both the half-light radius and the UV star formation rate are comparable to the typical values found for Lyman break galaxies at $z \sim 4 - 5$. The Ly α emitters are sub- L^* galaxies, with deduced star formation rates of $1 - 10 M_{\odot} \text{ yr}^{-1}$. One of the Ly α emitters is only detected in Ly α . Based on the star formation rate of $\sim 3 M_{\odot} \text{ yr}^{-1}$ calculated from Ly α , the lack of continuum emission could be explained if the galaxy is younger than $\sim 2 \text{ Myr}$ and is producing its first stars.

Observations in $V_{606}i_{775}z_{850}$ were used to identify additional Lyman break galaxies associated with this structure. In addition to the radio galaxy, there are 22 V_{606} -break ($z \sim 5$) galaxies with $z_{850} < 26.5$ (5σ), two of which are also in the spectroscopic sample. We compare the surface density of $\sim 2 \text{ arcmin}^{-2}$ to that of similarly selected V_{606} -dropouts extracted from GOODS and the UDF Parallel fields. We find evidence for an overdensity to very high confidence ($> 99\%$), based on a counts-in-cells analysis applied to the control field. The excess is suggestive of the V_{606} -break objects being associated with a forming cluster around the radio galaxy.

Subject headings: cosmology: observations – early universe – large-scale structure of universe – galaxies: high-redshift – galaxies: clusters: general – galaxies: starburst – galaxies: individual (TN J0924–2201)

1. Introduction

Where can we find the progenitors of the galaxy clusters that populate the local Universe? The evolution of rich galaxy clusters has been studied out to $z \sim 1.4$ (Mullis et al. 2005). These clusters have been discovered primarily via their bright X-ray emission, the signature of virialised gas within a deep gravitational potential well. Follow-up observations have revealed that some of the galaxy populations in distant clusters are relatively old, as evidenced by, for example, the tight scatter in the color-magnitude relation for early-type galaxies (e.g. Stanford et al. 1998; Blakeslee et al. 2003a; Wuyts et al. 2004; Holden et al. 2005), and the mild evolution of the morphology density relation for cluster ellipticals since $z \sim 1$ (Postman et al. 2005). This suggests that an interesting epoch of cluster forma-

tion could lie at higher redshifts. Several good examples for overdensities of galaxies at $1.5 \lesssim z \lesssim 6$, possibly the progenitors of clusters, exist in the literature (e.g. Pascarelle et al. 1996; Steidel et al. 1998; Keel et al. 1999; Steidel et al. 2000; Francis et al. 2001; Möller & Fynbo 2001; Sánchez & González-Serrano 2002; Shimasaku et al. 2003; Ouchi et al. 2005; Steidel et al. 2005). These structures have been found often as by-products of large-area field surveys using broad or narrow band imaging, or by targeting luminous radio sources.

One technique for finding distant galaxy overdensities is based on the empirical evidence that powerful radio galaxies are among the most massive forming galaxies at high redshift (e.g. De Breuck et al. 2002; Dey et al. 1997; Pentericci et al. 2001; Zirm et al. 2003). In the standard cold dark matter (CDM) universe model, massive galaxies and galaxy clusters are associated with the most massive dark matter haloes within the large-scale structure. It has been found that massive black holes are a key-ingredient of local massive galaxies, and that their mass scales in proportion to the mass of the spheroidal component of the host galaxy (Magorrian et al. 1998; Gebhardt et al. 2000; Ferrarese & Merritt 2000). Radio galaxies may therefore demarcate the location of forming clusters, analogous to the suggested scaling relations between halo, host galaxy and black hole mass at low redshift. A program with the Very Large Telescope (VLT) of the European Southern Observatory to search for galaxy overdensities around luminous high-redshift radio galaxies through deep narrow band Ly α imaging and spectroscopy has indeed revealed that the radio galaxies are often accompanied by large numbers of line emitting galaxies (Pentericci et al. 2000; Kurk et al. 2003; Venemans et al. 2002, 2004, 2005).

We have started a study with the *Advanced Camera for Surveys* on the Hubble Space Telescope (HST/ACS; Ford et al. 1998) to survey some of these Ly α -selected *protoclusters*¹. Our goal is to augment our study of emission line objects by deep broad band observations to search for Lyman break galaxies (LBGs). Observations of the radio galaxy protocluster TN J1338–1942 at $z = 4.1$ have shown that the overdensity of Ly α emitters discovered by Venemans et al. (2002) is accompanied by a similar overdensity of Lyman break galaxies, allowing us to assess distinct galaxy populations in overdense regions (Miley et al. 2004, Overzier et al., in prep.). The radio galaxy TN J1338–1942 was found to have a complex morphology, showing clear signs of AGN feedback on the forming ISM and a starburst-driven wind possibly feeding the gaseous halo that surrounds the galaxy (Zirm et al. 2005). The Ly α emitters have relatively faint UV continua and small angular sizes compared to the generally brighter LBG population in field studies (e.g. Ferguson et al. 2004; Bouwens et al.

¹The term *protocluster* has no strict definition in literature. It is commonly used to describe galaxy overdensities at high redshift with mass estimates that are comparable to those of galaxy clusters, but without any detectable X-ray emission from a hot, virialised intra-cluster medium.

2004a).

TN J0924–2201 at $z = 5.19$ is the most distant radio galaxy known (van Breugel et al. 1999; De Breuck et al. 2000). Following the successes obtained in identifying Ly α galaxy overdensities around our sample of powerful high redshift radio galaxies at $2.2 < z < 4.1$, Venemans et al. (2004) have probed the distribution of Ly α emitters around TN J0924–2201: there are 6 spectroscopically confirmed companions within a (projected) radius of 2.5 Mpc and a (rest-frame) 1000 km s^{-1} from the radio galaxy, corresponding to a surface overdensity of 1.5–6 with respect to the field. This overdensity is comparable to that of radio galaxy/Ly α protoclusters at lower z , and is in support of the idea that radio galaxies conspicuously identify groups or cluster-like regions in the very early Universe.

In this paper we present the results of a follow-up study of the galaxy overdensity near TN J0924–2201 through high resolution imaging observations obtained with HST/ACS. The primary goal of these observations was to look for an enhancement in the surface density of Lyman break galaxies in the field of TN J0924–2201, which would generally be missed by the selection based on the presence of a Ly α emission line alone. LBGs and Ly α emitters are strongly clustered at $z = 3 - 5$, and are highly biased relative to predictions for the dark matter distribution (Giavalisco et al. 1998; Adelberger et al. 1998; Ouchi et al. 2004b). The biasing becomes stronger for galaxies with higher rest-frame UV luminosity (Giavalisco & Dickinson 2001). In an excellent, all-encompassing census of the clustering properties of LBGs, Ouchi et al. (2004b) found that the bias may also increase with redshift and dust extinction, in addition to UV luminosity. By comparing the number densities of LBGs to that of dark halos predicted by Sheth & Tormen (1999) they concluded that $z = 4$ LBGs could be hosted by halos of $1 \times 10^{11} - 5 \times 10^{12} M_{\odot}$ (see also Hamana et al. 2004), and that the descendants of those halos at $z = 0$ have masses that are comparable to the masses of groups and clusters.

The structure of this paper is as follows. In Section 2 we describe our observations and data analysis. Section 3 subsequently deals with the host galaxy of the radio source, the spectroscopically confirmed Ly α emitters, and our sample of $z \sim 5$ Lyman break galaxies. In Section 4 we discuss the evidence that suggests that TN J0924–2201 may pinpoint a young galaxy cluster, and we present our conclusions in Section 5. We use a cosmology in which $H_0 = 72 \text{ km s}^{-1} \text{ Mpc}^{-1}$, $\Omega_M = 0.27$, and $\Omega_{\Lambda} = 0.73$ (Spergel et al. 2003). In this Universe, the luminosity distance is 49.2 Gpc and the angular scale size is $6.2 \text{ kpc arcsec}^{-1}$ at $z = 5.2$. The lookback time is 12.2 Gyr, corresponding to an epoch when the Universe was approximately 8% of its current age.

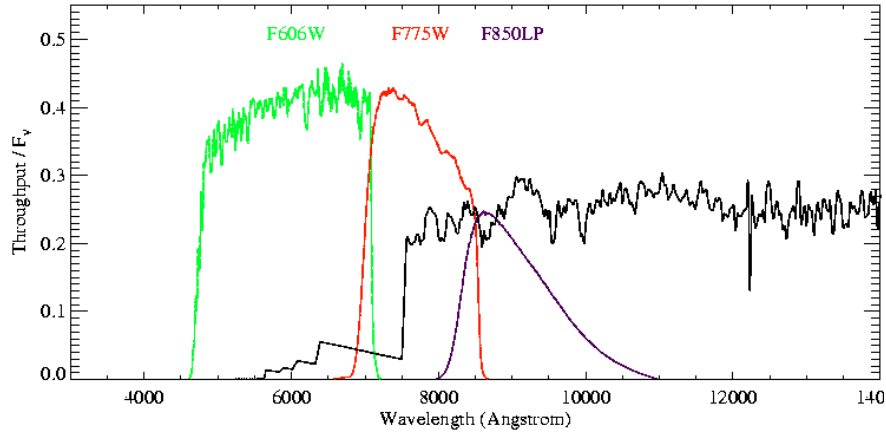


Fig. 1.— Total effective throughput of the HST/ACS filterset used in our observations. The SED template shown is the *SB2* template from Benítez (2000), redshifted to $z = 5.19$ taking into account the attenuation of the IGM following the prescription of Madau et al. (1996). The Lyman break occurs between filters V_{606} and i_{775} for galaxies at $z \sim 5$.

2. ACS Observations, data reduction and photometry

2.1. TN J0924–2201

We surveyed the field surrounding TN J0924–2201 with a single pointing of the Wide-Field Channel (WFC) of HST/ACS. The field position was chosen in order to maximize the number of spectroscopically-confirmed Ly α emitters in the field. The radio galaxy is located at $\alpha_{J2000} = 9^h 24^m 19.90^s$, $\delta_{J2000} = -22^\circ 01' 42.0''$, and 4 of the Ly α emitters fall within the 11.7 arcmin² field. The field has an extinction value $E(B - V) = 0.057$ determined from the dust maps of Schlegel et al. (1998). The observations were carried out between 29 May and 8 June 2003, as part of the ACS Guaranteed Time Observing (GTO) high redshift cluster program. The total observing time of 14 orbits was split over the V_{606} (9400 s), i_{775} (11800 s) and z_{850} (11800 s) broad-band filters, bracketing redshifted Ly α at 7527 Å. The filter transmission curves are indicated in Fig. 1. Each orbit was split into two 1200 s exposures to facilitate the removal of cosmic rays. A color image of the field is shown in Fig. 2.

The data were processed through CALACS at STScI and the ACS pipeline science investigation software *Apsis* (Blakeslee et al. 2003b) that was developed by and for the ACS GTO team. By default *Apsis* provides final drizzled images with a pixel scale of 0''.05 pixel⁻¹. However, to match the image scale of the public data release of the GOODS data (our main comparison dataset), we drizzled the science images onto a frame with a pixel scale of 0''.03 pixel⁻¹. Fig. 3 (left panels) shows the limiting magnitudes for each filter as a function of



Fig. 2.— ACS color image showing V_{606} in blue, i_{775} in green and z_{850} in red. The field measures 11.7 arcmin^2 . The approximate position of the radio galaxy is marked ‘RG’.

aperture diameter and signal-to-noise. The 2σ limiting magnitudes in a square aperture of 0.2 arcsec^2 are ~ 29.0 in V_{606} , ~ 28.5 in i_{775} , and ~ 28.0 in z_{850} . There is no significant difference in the detection limits for the $0''.05 \text{ pixel}^{-1}$ dataset and the $0''.03 \text{ pixel}^{-1}$ dataset. The total filter exposure times, extinctions and zeropoints (Sirianni et al. 2005) are listed in Table 1.

2.2. GOODS public data

We used the public imaging data from the Great Observatories Origins Deep Survey (GOODS; Giavalisco et al. 2004b) as a control field for our data. Similar to TN J0924–2201, GOODS has observations in V_{606} , i_{775} and z_{850} , and is comparably deep. We downloaded

the V1.0 mosaicked images release² for the GOODS Chandra Deep Field South (CDF-S) and Hubble Deep Field North (HDF-N) regions. Details on how these images were produced can be found in Giavalisco et al. (2004b). In total we used an area of ~ 314 arcmin² from this survey (see Section 4.1), roughly $27\times$ larger than a single ACS pointing. We used the zeropoints given by Giavalisco et al. (2004b) for this dataset. Fig. 3 (bottom panels) shows that the depth is comparable to that of our TN J0924–2201 observations. A summary of the GOODS observations are provided in Table 1.

2.3. UDF parallels

We also used the two ACS parallels to the Hubble Ultra Deep Field (UDF) NICMOS observations (GO-9803; R. I. Thompson et al.) for comparison³. The observations consist of 2 parallel fields with pointings of $\alpha_{J2000} = 3^h32^m46.0^s$, $\delta_{J2000} = -27^\circ54'42.3''$ (UDF-P1) and $\alpha_{J2000} = 3^h32^m1.0^s$, $\delta_{J2000} = -27^\circ48'3.5''$ (UDF-P2). The heavily dithered images were trimmed down to only the central regions covering 11.7 arcmin² for each parallel field. The data were reduced using *Apsis* at the default output scale of $0''.05$ pixel⁻¹. The UDF parallels reach about 0.5–1 magnitudes deeper in each filter compared to both TN J0924–2201 and GOODS (see Fig. 3). Details on the observations are given in Table 1.

2.4. Object detection and photometry

Object detection and photometry was done using the Source Extractor (SExtractor) software package of Bertin & Arnouts (1996). We used SExtractor in double-image mode, where object detection and aperture determination are carried out on the so-called “detection image”, and the photometry is carried out on the individual filter images. The z_{850} -band was used as the detection image. Photometric errors are calculated using the root mean square (RMS) images that contain the final error per pixel for each output science image. The RMS images correctly reflect the pixel variation when images are stacked in the absence of non-integer pixel shifts or corrections for the geometric distortion. For the fields at a scale of $0''.03$ pixel⁻¹ (TN J0924–2201 and GOODS), the main parameters influencing the detection and photometry are essentially the same as the parameters that were used to construct the GOODS ‘r1.1z’ public dataset source catalogue (see Giavalisco et al. 2004b):

²<http://www.stsci.edu/science/GOODS/>

³Available through MAST (<http://archive.stsci.edu/>)

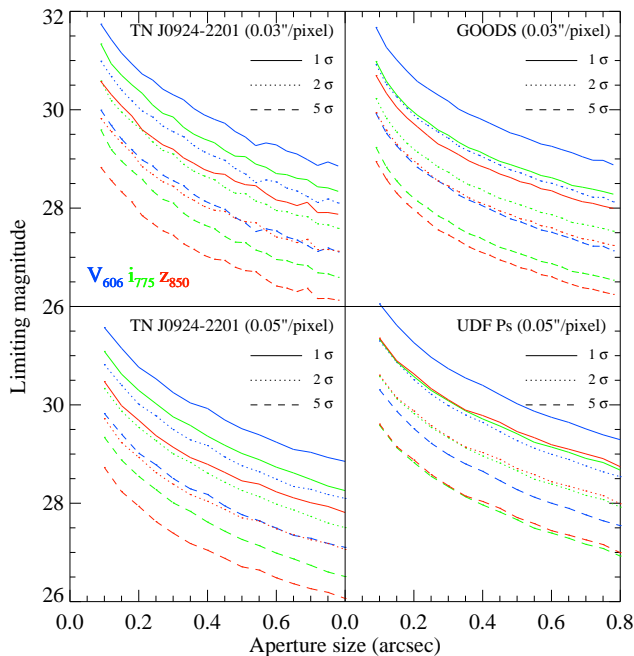


Fig. 3.— Depth as a function of square aperture diameter for the different datasets. Curves give the 1σ (solid), 2σ (dotted), and 5σ (dashed) limiting magnitudes in V_{606} (blue), i_{775} (green), and z_{850} (red).

we initially considered all detections with a minimum of 16 connected pixels each containing >0.6 times the standard deviation of the local background (giving a signal-to-noise ratio (S/N) of >2.4). SExtractor’s deblending parameters were set to `DEBLEND_MINCONT` = 0.03, `DEBLEND_NTHRESH` = 32. The publicly available inverse variance images provided by the GOODS team were converted to RMS images to ensure that the absolute standard deviations per pixel are used by SExtractor. For the UDF Parallel datasets that were drizzled at a scale of $0''.05 \text{ pixel}^{-1}$, we detected objects using a minimum of 5 connected pixels at a threshold of 1.1 times the RMS of the local background (nominal S/N of >2.4) and setting `DEBLEND_MINCONT` = 0.1 and `DEBLEND_NTHRESH` = 8.

After this initial detection we rejected all objects with S/N less than 5 in z_{850} , where we define S/N as the ratio of counts in the isophotal aperture to the errors on the counts. The remaining objects were considered real objects. Galactic stars appear to closely overlap with galaxies in the $V_{606}-i_{775}$, $i_{775}-z_{850}$ color-color plane (see section 3.4). We initially rejected all point sources on the basis of high SExtractor stellarity index, e.g., setting $S/G < 0.85$ (non-stellar objects with high confidence).

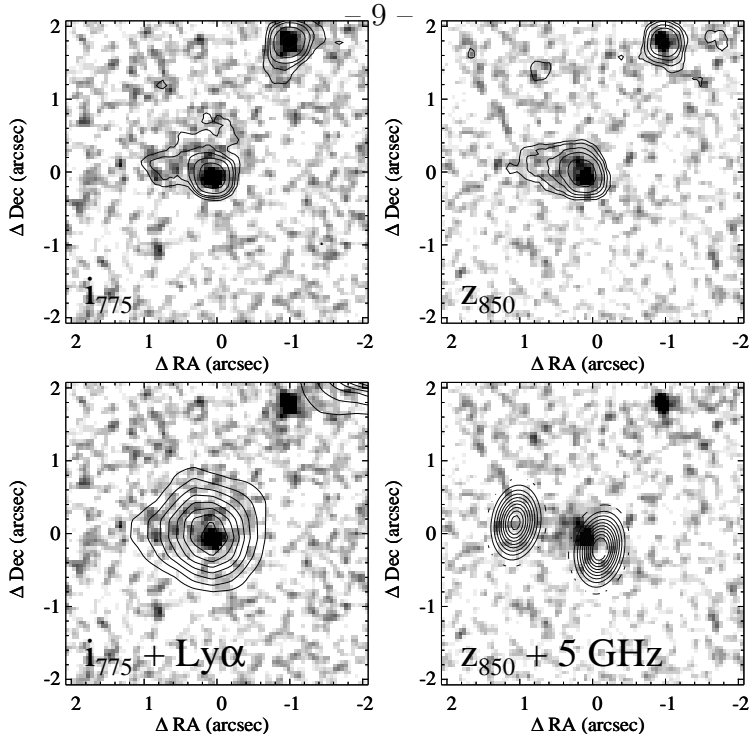


Fig. 4.— HST/ACS images of radio galaxy TN J0924–2201. *Top left:* i_{775} with contours of the same image smoothed using a $0.15''$ (FWHM) Gaussian to enhance the faint ‘tail’. *Top right:* Same as Top left, but for the z_{850} -band. *Bottom left:* i_{775} -band image in greyscale with contours representing the ground-based narrow-band $\text{Ly}\alpha$ image (with a seeing of $\sim 0.8''$ (FWHM)). *Bottom right* z_{850} -band image in greyscale with contours of the 4.86 GHz radio image overlaid (C. De Breuck, private communications). Throughout this paper, all ACS greyscale postage stamps have been smoothed using a Gaussian kernel of $0.075''$ (FWHM). The continuum, the $\text{Ly}\alpha$, and the radio emission are all aligned.

We used SExtractor’s `MAG_AUTO` to estimate total object magnitudes within an aperture radius of $2.5 \times r_{\text{Kron}}$ (Kron 1980), but calculated *galaxy colors* from the isophotal magnitudes measured by SExtractor within the aperture defined by the isophotal area of the object in the z_{850} -band. These procedures are optimal for (faint) object detection and aperture photometry with ACS (Benítez et al. 2004). We measured half-light radii defined as that radius that contains half of the total light using annular photometry out to $2.5 \times r_{\text{Kron}}$ (performed by SExtractor). The total magnitudes and half-light radii have not been corrected for the amount of light missed outside the apertures, unless stated otherwise (see Benítez et al. 2004; Giavalisco et al. 2004b, Overzier et al., in prep. for aperture corrections applied to ACS observations). All colors and magnitudes quoted in this paper have been corrected for foreground extinction and are in the *AB* system of Oke (1971).

2.5. Photometric redshifts

We used the Bayesian Photometric Redshift code (BPZ) of Benítez (2000) to obtain estimates for galaxy redshifts, z_B . For a complete description of BPZ and the robustness of its results, we refer the reader to Benítez (2000) and Benítez et al. (2004). Our library of galaxy spectra is based on the elliptical, intermediate (*Sbc*) and late type spiral (*Scd*), and irregular templates of Coleman et al. (1980), augmented by starburst galaxy templates with $E(B - V) \sim 0.3$ (*SB2*) and $E(B - V) \sim 0.45$ (*SB3*) from Kinney et al. (1996), and two simple stellar population (SSP) models with ages of 5 Myr and 25 Myr from Bruzual & Charlot (2003). The latter two templates have been found to improve the accuracy of BPZ for very blue, young high redshift galaxies in the UDF (Coe et al., in prep.). BPZ makes use of a parameter ‘ODDS’ defined as $P(|z - z_B| < \Delta z)$ that gives the total probability that the true redshift is within an uncertainty Δz . For a Gaussian probability distribution a 2σ confidence interval centered on z_B would get an ODDS of > 0.95 . The empirical accuracy of BPZ is $\sigma \approx 0.1(1 + z_B)$ for objects with $I_{814} \lesssim 24$ and $z \lesssim 4$ observed in the $B_{435}V_{606}I_{814}$ -bands with ACS to a depth comparable to our observations (Benítez et al. 2004). Note that we will be applying BPZ to generally fainter objects at $z \sim 5$ observed in $(B_{435})V_{606}i_{775}z_{850}$. The true accuracy for such a sample has yet to be determined empirically.

3. Results

3.1. Radio galaxy TN J0924–2201

The radio galaxy was not detected in V_{606} due to the attenuation of flux shortward of $\text{Ly}\alpha$ by the intergalactic medium (IGM). We derive a 2σ upper limit of 28.3 magnitude within r_{Kron} . The galaxy is detected in the other filters with total magnitudes of $i_{775} = 26.0 \pm 0.1$ and $z_{850} = 25.5 \pm 0.1$, and colors of $V_{606} - i_{775} > 2.7$ and $i_{775} - z_{850} = 0.4 \pm 0.1$ (Table 2).

The radio galaxy’s $V_{606} - i_{775}$ color is affected by the relatively large equivalent width of $\text{Ly}\alpha$ ($EW_0 = 83 \text{ \AA}$, Venemans et al. (2004)). In the i_{775} - and z_{850} -bands, the galaxy consists of a compact object with a $\sim 1''$ ‘tail’ extending towards the East that we have made visible by smoothing the ACS images shown in Fig. 4 using a Gaussian kernel of $0''.15$ (FWHM). Also shown is the narrow-band $\text{Ly}\alpha$ from Venemans et al. (2004) in contours superposed on the ACS i_{775} -band (Fig. 4, bottom left). The narrow-band image was registered to the ACS image using a nearby star $\sim 3''$ to the northwest of the radio galaxy. The main component observed with ACS is entirely embedded in the $\sim 1''.5$ (~ 9 kpc) $\text{Ly}\alpha$ halo (compared to a seeing of $0.8''$). The lower right panel of Fig. 4 shows the VLA 4.86 GHz radio contours (C. De Breuck, private communications), overlaid on the ACS z_{850} -band image. The relative as-

trometry could not be determined to better than $0''.5$. We find good correspondence between the orientations of the radio emission and the extended ACS emission. This is analogous to the alignment of both the UV continuum and emission lines with the radio seen in other HzRGs at lower redshifts, which can be due to (a combination of) scattered light, emission lines and, possibly, jet-induced star formation (e.g. Best et al. 1998; Bicknell et al. 2000; Zirm et al. 2005, and references therein). Several emission lines common to high-redshift radio galaxies fall within the z_{850} transmission curve (CIV $\lambda 1549\text{\AA}$, HeII $\lambda 1640\text{\AA}$). Based on a composite radio galaxy spectrum, we estimate that the contribution due to these lines is at most ~ 0.2 mag in z_{850} . If the continuum is further dominated by the emission of young, hot stars with little dust, we derive a star formation rate (SFR) of $13.3 M_{\odot} \text{ yr}^{-1}$. This SFR is comparable to that of normal star-forming galaxies at $z \sim 4 - 6$ (e.g. Steidel et al. 1999; Papovich et al. 2001; Ouchi et al. 2004a; Giavalisco et al. 2004a; Bouwens et al. 2004b).

3.2. Properties of Ly α emitting galaxies at $z \approx 5.2$

In this section we will study some of the properties of the four Ly α emitting galaxies from Venemans et al. (2004). The morphologies in the 3 bands are shown in Fig. 5, and their photometric properties are summarized in Table 2. All four Ly α emitters were detected in i_{775} , the filter that includes Ly α , with one object (#2688) being solely detected in this filter. The UV continuum magnitudes measured from the z_{850} -band are all fainter than 25.8 magnitudes, making them fainter than the faintest galaxies in the $z \sim 5$ GOODS LBG sample from Ferguson et al. (2004). This implies that this population of Ly α galaxies is confined to luminosities of $\lesssim 0.7 L^*$, where L^* is the characteristic continuum luminosity of $z = 3$ LBGs from Steidel et al. (1999). Two emitters have a luminosity of $\lesssim 0.3 L^*$. It is evident that the selection of these Ly α galaxies is biased in two important ways. One, the sample is naturally biased towards galaxies with high equivalent width of Ly α , and second, it is biased towards the fainter end of the Lyman break galaxy luminosity function. This finding seems consistent with that of Shapley et al. (2003) who found evidence that Ly α equivalent width increases towards fainter continuum magnitudes in their spectroscopic $z \sim 3$ LBG sample. The faint UV continuum of these Ly α emitting galaxies is similar to that observed for Ly α galaxies associated with other radio galaxies (Venemans et al. 2004; Miley et al. 2004, Overzier et al., in prep.).

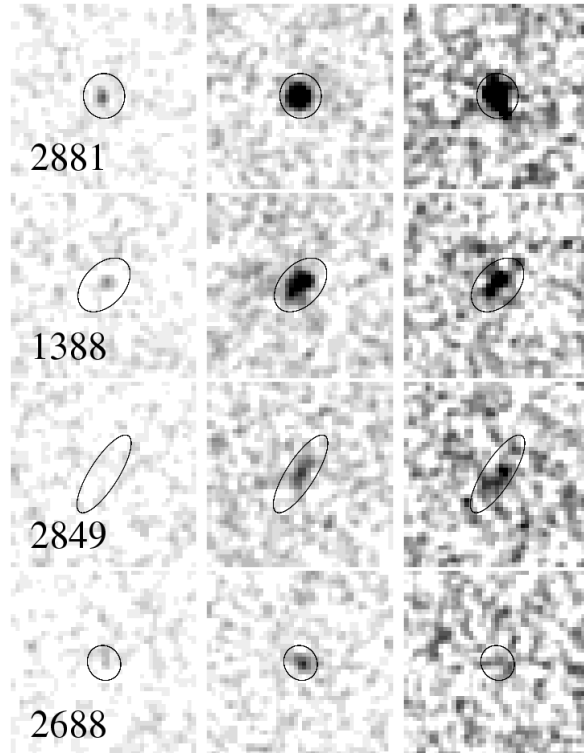


Fig. 5.— V_{606}, i_{775} and z_{850} (from left to right) images of the four spectroscopically confirmed Ly α emitters of Venemans et al. (2004). The images have been smoothed using a Gaussian kernel of $0.075''$ (FWHM). Kron apertures determined from the i_{775} -band image are indicated. The images are $2'' \times 2''$ in size.

3.2.1. Continuum slopes

We can use the accurate ACS photometry together with the narrow-band Ly α flux densities to try to sharpen the constraints on the Ly α EW and to determine the continuum slope ($f_{\lambda} \propto \lambda^{\beta}$) of these emitters. To this end, we follow the procedures detailed in Venemans et al. (2005) to subsequently derive the UV slope β , the strength of the continuum, the contribution of Ly α to i_{775} , and its (rest-frame) equivalent width, EW_0 . We take into account that for a source at $z = 5.2$ a fraction $Q_{775} \approx 0.68$ of the i_{775} flux is absorbed by intervening neutral hydrogen (Madau 1995), and note that this fraction is virtually independent of β . The uncertainties on β and EW_0 were obtained by propagating the individual errors on the measured magnitudes using a Monte Carlo method, and fitting the resulting distributions with a Gaussian. For object #2881, the brightest in our sample, we find good constraints on both the UV slope and the Ly α EW, $\beta = -0.8 \pm 0.6$ and $EW_0 = 39 \pm 7$. The continuum

seems redder than the average slope of $\beta = -1.8 \pm 0.2$ of V_{606} -dropouts in GOODS found by Bouwens et al. (2005b). However, we can not rule out the possibility that the Ly α flux in i_{775} has been over-subtracted due to the presence of faint, extended Ly α in the VLT narrow-band Ly α image (PSF of $\sim 0''.8$) not detected with ACS (PSF of $\sim 0''.1$). This could have caused the slope calculated above to be shallower than it in fact is. We were not able to place tight constraints on the two fainter objects #1388 and #2849 detected in i_{775} and z_{850} , and refer to Venemans et al. (2005) who find $EW_0 \sim 50 \text{ \AA}$ with large errors under the assumption of a flat (in f_ν , i.e., $\beta = -2$) spectrum.

3.2.2. Star formation rates

Using the emission-line free UV flux at 1500\AA measured in z_{850} , we derive star formation rates using the conversion between UV luminosity and SFR for a Salpeter initial mass function (IMF) given in Madau et al. (1998):

$$\text{SFR} = \frac{L_{1500\text{\AA}} [\text{erg s}^{-1}\text{Hz}^{-1}]}{8 \times 10^{27}} M_\odot \text{ yr}^{-1} \quad (1)$$

We find 5.9 and 3.0 $M_\odot \text{ yr}^{-1}$ for objects #1388 and #2849. Object #2881 has a SFR of 9.7 $M_\odot \text{ yr}^{-1}$, quite comparable to that derived for the radio galaxy (see Sect. 3.1). These SFRs are considered to be lower limits, since the presence of dust is likely to absorb the (rest-frame) UV luminosities observed. The Ly α -to-continuum SFR ratios are in the range 0.7–3. The Ly α SFRs were derived following the standard assumption of case B recombination, valid for gas that is optically thick to HI resonance scattering (Venemans et al. 2005).

As modeled by Charlot & Fall (1993), high equivalent width Ly α is expected for a relatively brief period in young ($\sim 10^{7-9}$ yr), nearly dust-free galaxies. However, the general understanding is that, regardless of the effects of dust, the UV continuum is a better probe of the SFR than Ly α , given the large cross-section to resonance scattering for the latter. While the Ly α profile can be severely diminished depending on the geometry of the system, the gas density, and the dust contents, the *enhancement* of Ly α flux over UV flux is also not ruled out, at least theoretically. Young galaxies may consist of a 2-phase medium (e.g. Rees 1989) effectively thin to Ly α photons scattering off the surfaces of clouds that are optically thick to unscattered UV photons (Neufeld 1991). For the Ly α emitters found in overdensities associated with radio galaxies we find that the star formation rates derived from the UV and Ly α are generally of a similar order of magnitude (e.g., this paper, Venemans et al. 2005, Overzier et al., in prep.). It is unlikely that geometry, dust and scattering medium all conspire so that the SFRs derived from Ly α and the continuum will be comparable. More

likely it implies that both the UV and Ly α offer a relatively clear view (e.g. little dust and simple geometry) towards the star-forming regions of these galaxies.

3.2.3. Sizes

Except for source #2688, which we will discuss in detail below, the sources are (slightly) resolved in i_{775} and z_{850} . The half-light radii measured in z_{850} are $0''.10$ – $0''.16$, implying that the (projected) physical half-light diameters are <2.5 kpc, where we have applied a correction for the degree to which half-light radii as measured by SExtractor are underestimated for objects with $z_{850} \approx 26$ based on profile simulations (Overzier et al., in prep). The sizes are comparable to the sizes we have measured for Ly α emitters associated with radio galaxies at $z = 3.13$ and $z = 4.11$ (Miley et al. 2004; Venemans et al. 2005, Overzier et al. in prep.). We find no evidence for dominant active nuclei among these Ly α emitters.

3.3. A galaxy without UV continuum

Object #2688 from Venemans et al. (2004) is particularly interesting. It is the faintest object in our Ly α sample ($i_{775} \approx 28$) and it is not detected in z_{850} at the 2σ level ($z_{850} > 28.4$). Likewise, there is no detection in V_{606} . Assuming $\beta \approx -2$, which is appropriate for a dustless, young (1–100 Myr) galaxy, correcting for the Ly α emission in the i_{775} -band would place this object’s magnitude close to the detection limit in i_{775} . This implies that the i_{775} flux is solely that of Ly α , with an EW_0 of > 100 Å. What physical processes could explain its peculiar observed properties?

- **Young star-forming galaxy?** If object #2688 is a young star-forming galaxy, the observed equivalent width of Ly α should be a function of the age of the stellar population. Venemans et al. (2004) estimated the star formation rate in #2688 from its Ly α luminosity and found $\sim 3 M_{\odot} \text{ yr}^{-1}$. Based on a population synthesis model for a young stellar population with a SFR of $3 M_{\odot} \text{ yr}^{-1}$ (Salpeter IMF, $M_l = 1M_{\odot}$, $M_u = 100M_{\odot}$) shown in Fig. 6, our robust limit on the z_{850} -band (~ 1465 Å rest-frame) would be surpassed within only ~ 2 Myr (Leitherer et al. 1999). A comparably young object was found by Ellis et al. (2001) at $z = 5.6$. In this case, the lensing amplification by the cluster Abell 2218 also enabled to place a strong upper-limit on the object size of 150 pc, consistent with it being a typical HII region. Given the non-detection of #2688 in z_{850} , it is difficult to place an upper limit on the size of the object. If we take the physical half-light diameter of 2.5 kpc derived for the other Ly α emitters as an extreme upper limit on the size, it is not likely that star formation

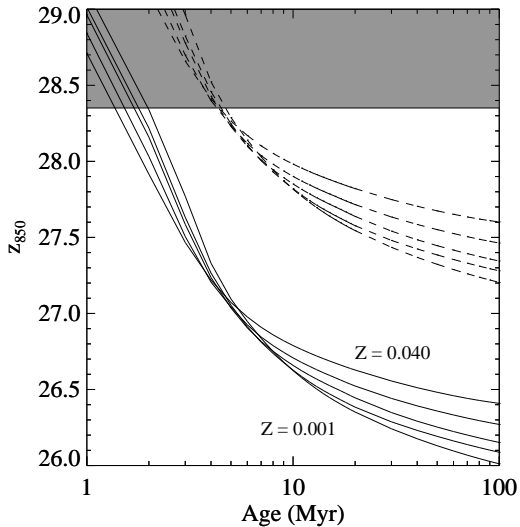


Fig. 6.— The z_{850} continuum magnitude as a function of age for a continuous star formation model with a SFR of $3 M_{\odot} \text{ yr}^{-1}$ from STARBURST99 (Leitherer et al. 1999) (Salpeter IMF with $M_l = 1 M_{\odot}$, $M_u = 100 M_{\odot}$). The metallicities of the models are 0.001, 0.004, 0.008, 0.02, and 0.04 (from bottom to top). The shaded box demarcates the 2σ limit on the z_{850} magnitude within the Kron aperture of Ly α emitter #2688. Dashed lines indicate similar models, but with a SFR of only $1 M_{\odot} \text{ yr}^{-1}$. The non-detection in z_{850} may indicate that #2688 has an age of only a few Myr.

can progress over such large size within only a few Myr. Whether the actual size of the Ly α emitting in #2688 is similar to that of typical HII regions is unclear given the extremely thin detection in i_{775} .

- **Outflow?** Extended emission line regions seem to be a common feature of both local and high-redshift star-forming galaxies. Locally, some of the emission is produced in galactic scale outflows. Empirically there is a lower limit to the surface density of star formation necessary to launch such a galactic wind of $0.1 M_{\odot} \text{ yr}^{-1} \text{ kpc}^{-2}$ (Heckman et al. 1990). For #2688 we calculate a star formation rate surface density of $> 0.5 M_{\odot} \text{ yr}^{-1} \text{ kpc}^{-2}$. Therefore, the observed high equivalent-width Ly α may be a result of outflowing gas, while the galaxy itself may be obscured and older than the strong upper limit of a few Myr derived for the above scenario.

- **AGN?** The equivalent width of Ly α could also be boosted by the presence of an active nucleus. TN J0924–2201 itself has a Ly α $EW_0 = 83 \text{ \AA}$ close to the lower limit derived

for #2688. While there is no evidence for a bright nuclear point-source in #2688, it could be easily obscured by circumnuclear dust, particularly at rest-frame ultraviolet wavelengths. Because the spectrum only has narrow Ly α , it could be a faint narrow line quasar. Several of the Ly α emitters in the protocluster near radio galaxy MRC 1138–262 at $z = 2.16$ have been detected with *Chandra* indicating that the AGN fraction of such protoclusters could be significant. In contrast, Wang et al. (2004) found no evidence for AGN among a large field sample of $z \approx 4.5$ Ly α emitters observed in the X-ray.

3.4. Selection of V_{606} -dropouts

Galaxies without a significant excess of Ly α (i.e. rest-frame $EW_{Ly\alpha} < 20\text{\AA}$) constitute $\sim 75\%$ of LBG samples (Shapley et al. 2003), and hence are missed by selection purely based on the presence of Ly α emission. To circumvent this inherent bias in Ly α surveys, galaxies can be selected on the basis of broad-band colors that straddle the Lyman break for some specific redshift range. Unfortunately, having only a few filters, the Lyman break selection provides only a crude selection in redshift space due to photometric scatter and uncertainty in the underlying spectral energy distributions. This is especially important when we want to test for the presence of LBGs within a relatively narrow redshift range of the radio galaxy.

Giavalisco et al. (2004a) selected V_{606} -dropouts from the GOODS fields using the criteria:

$$\begin{aligned} & [(V_{606} - i_{775}) \geq 1.5 + 0.9 \times (i_{775} - z_{850}) \vee \\ & (V_{606} - i_{775}) \geq 2.0] \wedge (i_{775} - z_{850}) \leq 1.3 \wedge \\ & (V_{606} - i_{775}) \geq 1.2 \end{aligned} \quad (2)$$

where \vee and \wedge are the logical OR and AND operators. Although we will use these selection criteria to select V_{606} -dropout samples from our datasets, we will use a slightly modified selection window when discussing the clustering statistics of V_{606} -dropouts with respect to the radio galaxy (Section 4.1). We can tighten the color constraints given in Eq. 2 to effectively remove relatively blue objects that are likely to be at redshifts much lower than we are interested in ($z \approx 5.2$), as well as relatively red objects at much higher redshifts. We required

$$0.0 \leq (i_{775} - z_{850}) \leq 1.0 \quad (3)$$

in addition to Eq. 2 to reject galaxies at $z \lesssim 4.8$ and $z \gtrsim 5.5$, based on the color-color track of a 10^8 yr constant star forming model of $0.4Z_{\odot}$ metallicity. The resulting selection window is indicated in Fig. 7 (shaded area). The selection window of (Giavalisco et al. 2004a) as given in Eq. 2 has been indicated for comparison (dashed line).

Unlike GOODS and the UDF parallel fields, there are no observations in B_{435} for our field, which makes it impossible to remove low redshift contamination by requiring a maximum upper limit on detections in B_{435} (e.g., $S/N < 2$). The estimates for the low redshift contamination fraction of V_{606} -dropouts from GOODS amount to $\sim 10 - 30\%$ (Bouwens et al. 2005b). We note, however, that in some cases low redshift objects that have made it into the selection window can still be rejected on the basis of their high relative brightness and/or large sizes in the $V_{606}i_{775}z_{850}$ -bands during visual inspection.

3.5. Properties of V_{606} -dropouts in the field of TN J0924–2201

The $V_{606}-i_{775}$ versus $i_{775}-z_{850}$ diagram of the objects that meet our selection criteria is shown in Fig. 7 compared to the entire $V_{606}i_{775}z_{850}$ sample. Also shown are the color-color tracks of several standard SEDs and the stellar locus. We find 23 V_{606} -dropouts down to a limiting magnitude of $z_{850} = 26.5$. The radio galaxy (#1396) and the two brightest Ly α emitters (objects⁴ #449 and #1844) passed the V_{606} -dropout selection criteria. Table 3 lists the coordinates, colors and magnitudes of the LBG candidates. Fig. 8 shows the z_{850} -band image with the positions of the V_{606} -dropouts (blue circles) and the Ly α emitters (red squares).

3.5.1. SFRs and continuum slopes

Our limiting magnitude in z_{850} corresponds to $\sim 0.5 L^*$ (taking into account the average amount of flux missed). We calculated star formation rates from the emission-line free UV flux measured in z_{850} . The SFRs range from 5–42 $M_{\odot} \text{ yr}^{-1}$ if there is no dust (see Table 3). We calculated an average UV slope ($f_{\lambda} \propto \lambda^{\beta}$) for the entire sample from the $i_{775}-z_{850}$ color and find $\langle \beta \rangle = -2.4$ with a standard deviation of 1.7 for the sample. Here we have assumed a redshift of $z = 5.2$ to convert between magnitudes and the actual flux densities of the continuum in i_{775} . However, this assumed redshift is critical to the calculation of β , due to its large dependence on the amount of Ly α forest absorption in i_{775} : the average $i_{775}-z_{850}$ color corresponds to slopes ranging from $\langle \beta \rangle = -1.3$ at $z = 5.0$ to $\langle \beta \rangle = -4.0$ at $z = 5.4$. The average slope of $\langle \beta \rangle = -2.4$ that we measured is consistent with the average slope of V_{606} -dropouts ($\beta = -1.8 \pm 0.2$) in GOODS (Bouwens et al. 2005b).

It is impossible to fit both the redshift and the spectral slope independently. In the

⁴#2881 and #1388 in Table 2 and Venemans et al. (2004)

following we will assume that $z = 5.2$, and that the value of the spectral slope is largely determined by dust, rather than age or metallicity. We have parametrized $E(B - V) - \beta_{iz}$ for a base template consisting of a 100 Myr old ($z_f \approx 5.6$) SED with $0.2 Z_\odot$ metallicity that has been forming stars at a continuous rate (from Bruzual & Charlot 2003). The template was reddened by applying increasing values of $E(B - V)$ using the recipe of Calzetti et al. (2000). The measured slopes are consistent with modest absorption by dust of $E(B - V) \sim 0 - 0.4$, with the lower values preferred given the mean slope of the sample. In some cases we also found negative values of $E(B - V)$. This suggests that the color might be bluer than that of the base template used, or that the redshift is off.

Bouwens et al. (2005b) found evidence for evolution in the mean UV slope from $z \sim 5$ ($\beta = -1.8 \pm 0.2$) to $z \sim 2.5$ ($\beta = -1.4 \pm 0.1$) (see also Lehnert & Bremer 2003; Ouchi et al. 2004a; Papovich et al. 2004; Bouwens et al. 2005a). They have interpreted this as an evolution in the dust content rather than age or metallicity, based on the plausible assumption that any change in these parameters by significantly large factors seems unlikely given that the universe only doubles in age over this redshift interval and the gradual process of galaxy formation. Reducing the dust content by a factor of ~ 2 from $z \sim 3$ to $z \sim 5$ can explain the relatively blue continuum of the V_{606} -dropouts.

3.5.2. Sizes

We have measured half-light radii in z_{850} . A Gaussian fit to the size distribution gives a $\langle r_{hl,z} \rangle = 0''.16$ with standard deviation $0''.05$. The mean half-light radius corresponds to ~ 1.2 kpc at $z \sim 5$. Note that our sample is biased against $z \sim 5$ AGN point sources, since they would be rejected based on their high stellarities. If we divide our sample in two magnitude ranges $z_{850} = 24.2 - 25.5$ and $z_{850} = 25.5 - 26.5$, the mean half-light radii for the two bins are $0''.20$ and $0''.14$, respectively.

While it cannot entirely be ruled out that fainter LBGs are intrinsically smaller, the observed difference between the two bins can most likely be explained by the effect of surface brightness dimming in two ways: 1) the fraction of light that is missed in aperture photometry is larger for fainter sources, and 2) the incompleteness is higher for larger sources at a fixed magnitude (see e.g. Bouwens et al. 2004b; Giavalisco et al. 2004b). The mean half-light radius of $z_{850} < 25.8$ LBGs at $z \sim 5$ in GOODS is $\langle r_{hl,z} \rangle \approx 0''.27$, as measured by Ferguson et al. (2004). However, Ferguson et al. (2004) measured half-light radii using maximum apertures approximately $4\times$ larger than ours, which inevitably results in slightly larger half-light radii. Calculating the half-light radius using our method and our own sample of $z \sim 5$ LBGs from the GOODS field (Section 4.1) gives $\langle r_{hl,z} \rangle = 0''.17 \pm 0.06$ (with $0''.20 \pm 0.08$ and

$0''.16 \pm 0.05$ for the brighter and fainter magnitude bins, respectively), consistent with the sizes we find in the TN J0924–2201 field.

The V_{606} , i_{775} , and z_{850} morphologies are shown in Fig. 9. Three objects (#119, #303, and #444) have a clear double morphology. Based on the large V_{606} -dropout sample from GOODS (Section 4.1) we would expect roughly 1.5 of such systems in our field, indicating that our field might be relatively rich in merging systems. A more detailed, comparative analysis of sizes and morphologies of LBGs and Ly α emitters in radio galaxy protoclusters at $2 < z < 5.2$ will be given elsewhere.

3.5.3. Point sources

The Galactic stellar locus runs through our V_{606} -dropout selection window (green stars in Fig. 7). We found ~ 14 stellar objects that pass our selection criteria, if we let go of the requirement of relatively low stellarity index, as measured by SExtractor. However, the additional objects we found were all brighter than $z_{850}=25.0$, and the majority were scattered around the red end of the stellar locus. No new objects with high stellarity were found at fainter magnitudes. Therefore, we believe that we have not missed a significant population of (unresolved) $z \sim 5$ AGN in this field.

4. Discussion

4.1. An overdensity of V_{606} -dropouts associated with TN J0924–2201?

In this section we will test whether the overdensity of Ly α emitters near TN J0924–2201 found by Venemans et al. (2005) is accompanied by an overdensity of V_{606} -dropout galaxies. To establish what the surface density is of V_{606} -dropouts in the ‘field’ we have applied our selection criteria to the GOODS and the UDF Parallel fields. The color-color diagram for the objects in the GOODS fields is shown in Fig. 10. The GOODS and UDF Parallel fields cover a total area of ~ 337 arcmin² compared to ~ 12 arcmin² for TN J0924–2201. At $z_{850} < 26.5$ the numbers of V_{606} -dropouts satisfying our selection criteria are 277 for the combined GOODS fields, and 8 and 16 objects in the UDF-P1 and UDF-P2 fields, respectively. Similar to Bouwens et al. (2005b) we find that the number of V_{606} -dropouts is 10% higher in the HDF-N compared to the CDF-S due to cosmic variance. We derive an average surface density of 0.9 arcmin⁻² for the field, consistent with Giavalisco et al. (2004a) and the publicly available GOODS V1.1 catalogues which we have used to cross-check our results. The V_{606} -dropout surface density of 2.0 arcmin⁻² in the TN J0924–2201 field is twice

as high, while the overall object surface densities at $z_{850} < 26.5$, $S/N > 5$ and $S/G < 0.85$ are fairly constant: 106 arcmin^{-2} , 119 arcmin^{-2} and 98 arcmin^{-2} for the GOODS CDF-S, HDF-N, and TN J0924–2201 fields, respectively.

What is the significance of this factor 2 surface overdensity? LBGs are known to be strongly clustered at every redshift (Porciani & Giavalisco 2002; Ouchi et al. 2004b), and are known to have large field-to-field variations. In our particular case, it is interesting to calculate the probability of finding a certain number of V_{606} -dropouts in a single ACS pointing. Here we will use the additional constraint on the $i_{775}-z_{850}$ color specified in Eq. 3 and which is indicated by the shaded areas in Figs. 7 and 10. The angular distributions of the 218 GOODS V_{606} -dropouts satisfying these criteria are shown in Fig. 11. The distribution appears filamentary with noticeable ‘voids’ that are somewhat smaller than one ACS pointing. To the lower-left of the GOODS HDF-N mosaic in Fig. 11 we have indicated the size of a single $3'.4 \times 3'.4$ ACS pointing for comparison. We measured the number of LBGs in 1000 (500 for each GOODS field) square 11.7 arcmin^2 cells placed at random positions and orientation angles. The cells were allowed to overlap, and are therefore not totally independent. The histogram of counts-in-cells is shown in Fig. 12. The number of LBG candidates in TN J0924–2201 falls on the extreme right of the expected distribution based on GOODS (indicated by the red arrow). None of the cells randomly drawn from the CDF-S contained 19 objects (the highest being 14), while the chance of finding 19 objects in a single pointing in the HDF-N was slightly over 1%. Combining these results, TN J0924–2201 is overdense at the $> 99\%$ level with respect to GOODS.

As shown in Fig. 13, the excess in the TN J0924–2201 field over that of the GOODS sample (normalised to the same area) is primarily due to objects having $i_{775}-z_{850} \sim 0.0 - 0.5$. This clustering observed in the $i_{775}-z_{850}$ color distribution suggests that the significance of the surface overdensity is in fact much higher than the $> 99\%$ estimated above, given that $\sim 30\%$ of the GOODS V_{606} -dropouts populate the color diagram at $i_{775}-z_{850} > 0.5$, compared to only $\sim 10\%$ of the TN J0924–2201 candidates. The most significant number excess manifests itself around $i_{775}-z_{850} \approx 0.5$, which matches the expected color of an LBG spectrum at the redshift of the radio galaxy assuming a typical slope of $\beta \approx -2$ (the approximate redshift for such a template spectrum is indicated on the top axis of Fig. 13). Two of the three previously known protocluster members that are in the V_{606} -dropout sample also lie near this color (shaded regions in Fig. 13). Estimates of the photometric redshifts with BPZ also show a preference for $z \approx 5.2$ and slightly lower redshifts, although the errors on z_B are quite large (~ 0.7 , Fig. 14 & Table 3). The subclustering in $i_{775}-z_{850}$ and the photometric redshifts provide further evidence that the overdensity is associated with the radio galaxy and the $\text{Ly}\alpha$ emitters.

We can derive the V_{606} -dropout number densities from the comoving volume occupied by the objects. For the comoving volume one usually defines an effective volume, V_{eff} , that takes into account the magnitude and color incompletenesses. We estimated the effective redshift distribution, $N(z)$, associated with our selection criteria by running BPZ on the $B_{435}V_{606}i_{775}z_{850}$ photometry of the large GOODS V_{606} -dropouts sample. The redshift distribution is shown in Fig. 15, where we have also indicated the sum of the redshift probability curves of each object to maintain information on secondary maxima, as well as the uncertainties associated with each object. Our effective redshift distribution is slightly narrower than the redshift distribution of Giavalisco et al. (2004a) (indicated by the dashed line in Fig. 15), due to our additional constraint on $i_{775}-z_{850}$. Because we only used objects for which z_B was relatively secure (i.e., objects having $ODDS > 0.95$), as well as using the full z_B probability curves to construct Fig. 15, we believe that our $N(z)$ is a good approximation to the true underlying redshift distribution. While our $N(z)$ could appear too narrow if the errors on z_B are significantly underestimated, we can expect it to be narrower than that of Giavalisco et al. (2004a) in any case. The total probability of contamination seen around $z \sim 1$ amounts to $\sim 10\%$. This is similar to the number of objects in the GOODS sample for which the S/N in B_{435} is > 2 .

Using the effective $N(z)$ the comoving volume for the combined GOODS fields becomes $\sim 5.5 \times 10^5 \text{ Mpc}^3$. Here it is assumed that the selection efficiency at the peak of the redshift distribution is close to unity. Taking into account an incompleteness of $\sim 50\%$ for $z_{850} < 26.5$ (from Giavalisco et al. 2004a) gives an effective volume twice as small and a GOODS V_{606} -dropout volume density of $8 \times 10^{-4} \text{ Mpc}^{-3}$. For TN J0924–2201, the effective volume is $\sim 1 \times 10^4 \text{ Mpc}^3$ giving a number density of $2 \times 10^{-3} \text{ Mpc}^{-3}$ if all galaxies are spread out across the volume. If, on the other hand, a significant fraction (e.g., $\gtrsim 50\%$) of the objects are associated with the radio galaxy and Ly α emitters (assuming an effective protocluster volume of $8 \times 10^2 \text{ Mpc}^3$ at $\bar{z} = 5.2$ with $\Delta z = 0.03$), we find a volume density of $\gtrsim 1 \times 10^{-2} \text{ Mpc}^{-3}$ and a SFR density of $\gtrsim 1 \times 10^{-1} \text{ M}_\odot \text{ yr}^{-1} \text{ Mpc}^{-3}$. This is at least a tenfold increase compared to that of the field.

One may wonder what the cosmic variance implies for a field as large as GOODS. Somerville et al. (2004) have presented a useful recipe for deriving the cosmic variance based on the clustering of dark matter halos in the analytic CDM model of Sheth & Tormen (1999). Once the number density and mean redshift of a given population are known, one can derive the bias parameter, b , and calculate the variance of the galaxy sample, $\sigma_g = b\sigma_{DM}$, where σ_{DM} is the variance of the dark matter. A number density of $\sim 1 \times 10^{-3} \text{ Mpc}^{-3}$ corresponds to $b \approx 4$ and a variance $\sigma_{DM} \approx 0.07$ for dark matter haloes at $z \sim 5$. This would imply that the upper limit for the cosmic variance of V_{606} -dropouts in a field as large as one of the GOODS fields is $\sim 30\%$. The difference in the object densities that we found was $\sim 10\%$

between the two GOODS fields. Assuming that the CDF-S represents the absolute minimum of the allowed range would imply that new fields may be discovered showing significantly more sub-clustering on the scale of a single ACS pointing than currently observed. In the other extreme case that the HDF-N represents the absolute maximum, the TN J0924–2201 field should exhibit one of the highest surface densities of V_{606} -dropouts expected.

The surface overdensity of Ly α emitters around TN J0924–2201 was 1.5–6 compared to the field (Venemans et al. 2004). Our results would be marginally consistent with the lower value of ~ 2 . However, only two of the Ly α emitters are bright enough to be included in our LBG sample. If the fraction of LBGs with high rest-frame equivalent width Ly α in protoclusters is similar to that of the field (Shapley et al. (2003) find $\sim 25\%$), ~ 6 additional (i.e., non-Ly α) ‘protocluster’ LBGs are expected among our sample of 16 candidates (19 when including the radio galaxy and the two Ly α emitters). Such an overdensity could easily be accommodated given the relative richness of LBGs in this field, although its ultimate verification must await spectroscopic follow-up.

Based on the clustering statistics of relatively bright ($z' < 25.8$) $Vi'z'$ -selected LBGs at $z \sim 5$, Ouchi et al. (2004b) found that these objects are likely to be hosted by very massive dark matter halos of $\sim 10^{12} M_{\odot}$. The halo occupation number for these LBGs is almost unity, implying that almost every halo of this mass is expected to host a UV-bright LBG. Our sample contains several V_{606} -dropouts which have $z_{850} < 25.0$ (the brightest being #1873 with $z_{850} = 24.2$), implying present-day halo masses of $\langle M(z = 0) \rangle > 10^{14} M_{\odot}$. Whether any of these objects are associated with the radio galaxy should be confirmed by spectroscopy.

4.2. The host galaxy of TN J0924–2201

The high radio luminosity of TN J0924–2201 indicates that it hosts a supermassive black hole, which must have acquired its mass in less than ~ 1 Gyr. However, in many other respects we found that it appears unremarkable when compared to general Lyman break galaxies at a similar redshift. Although there is a wide dispersion in the properties of the highest redshift radio galaxies (e.g. Rawlings et al. 1996; Dey et al. 1997; Reuland et al. 2003; Zirm et al. 2005) it might be interesting to naively compare TN J0924–2201 to TN J1338–1942 at $z = 4.1$ also studied with ACS (Zirm et al. 2005). The optical host of TN J0924–2201 is almost 2 magnitudes fainter (at similar rest-frame wavelengths) than TN J1338–1941. There are several V_{606} -dropouts in our sample that have brighter magnitudes (and therefore higher SFRs) than the radio source, while TN J1338–1942 is by far the brightest object among the sample of associated g_{475} -dropouts found in that field (Miley et al. 2004). Likewise, TN J0924–2201 has a size that is comparable to the average size

of V_{606} -dropouts (Bouwens et al. 2004b; Ferguson et al. 2004), while TN J1338–1942 is an exceptionally large ($\sim 2''$) galaxy. If TN J0924–2201 is to develop into a similar source within the ~ 400 Myr or so between $z \sim 5$ and $z \sim 4$, it would require an increase in the projected radio source size by a factor ~ 5 , in $\text{Ly}\alpha$ luminosity by a factor ~ 60 , in SFR by a factor of ~ 10 , and in UV size by at least a factor of 2. The recent detection of molecular gas (CO) by Klammer et al. (2005) suggests that there is $\sim 10^{11} M_{\odot}$ of (inferred) gas mass present. The rapid enrichment that brought about this reservoir of molecular gas could have been facilitated by the early formation of the radio source and the triggering of massive star formation. The amount of gas present shows that there is plenty of material available to sustain a high SFR of several $100 M_{\odot} \text{ yr}^{-1}$, possibly allowing this source to undergo dramatic changes in its UV luminosity and morphology during certain stages of its evolution.

5. Conclusions

We have presented statistical evidence for an overdensity of star forming galaxies associated with the radio galaxy TN J0924–2201. Our result is consistent with the overdensity of $\text{Ly}\alpha$ emitters discovered previously by Venemans et al. (2004), and is comparable to overdensities of $\text{Ly}\alpha$ emitters and Lyman break galaxies found around other high redshift radio galaxies. TN J0924–2201 could be a protocluster that will evolve into a cluster with a mass of $\sim 10^{14} M_{\odot}$ at $z = 0$.

The existence of relatively massive structures in the early Universe may not be uncommon, as suggested by, for example, the existence of quasars at even higher redshifts (e.g. Fan et al. 2003), the evidence for protoclusters out to $z < 6$, and the increasingly higher limit that can be set on the redshift of reionization. Regions of high mass concentrations are rare, strongly clustered objects at every redshift, that underwent high amplification since the initial conditions (Kaiser 1984). Radio galaxies are suspected to be the sites of the formation of a massive galaxy. The evidence reported of in this paper contributes to the hypothesis that redshift filaments and possibly groups or clusters of galaxies emerged together with these massive galaxies. In the radio-loud AGN unification model, the viewing angle relative to the jet determines whether a galaxy will be seen as a radio galaxy or as a radio-loud quasar (Barthel 1989). It is therefore expected that early galaxy overdensities could, in principle, also be found around high redshift radio-loud quasars. Results indicate that the same may hold for at least some radio-quiet quasars at $z > 5$ too (Djorgovski et al. 1999, 2003, Stiavelli et al. 2005).

Although primordial galaxy overdensities so far discovered are not solely limited to fields that contain a luminous AGN (e.g. Steidel et al. 1999; Ouchi et al. 2005), they hold a strong

connection to low redshift clusters due to the presence of a supermassive black hole and possibly a developing brightest cluster galaxy (Zirm et al. 2005). When the radio source has switched off, the host galaxy may become indistinguishable from other relatively massive, quiescent galaxies that may have been active in the past. The clustering properties and inferred halo masses of the brightest Lyman break galaxies suggest that their descendants at $z = 0$ fall into groups and clusters of galaxies (Ouchi et al. 2004b). Interestingly, the number densities of protoclusters, radio galaxies and Lyman break galaxy redshift spikes have all been found to be consistent with the abundance of local clusters (e.g. Steidel et al. 1999; Venemans et al. 2002; Ouchi et al. 2005, and references therein). Structures like TN J0924–2201 provide ideal comparisons with state-of-the-art N -body simulations. Springel et al. (2005) found that the descendants of the most massive objects at high redshift (presumed to be luminous quasars) can almost exclusively be identified with the most massive clusters at the current epoch. It might become possible to trace back cluster evolution from the well-studied regimes at $z \lesssim 1$ to slight overdensities at very high redshifts, possibly up to the epoch of reionization.

RAO is very grateful to Masami Ouchi for invaluable discussions, to Mike Dopita for discussion of Fig. 6, and to Carlos De Breuck for providing the radio map of TN J0924–2201 shown in Fig. 4. We thank the anonymous referee for helping to improve the manuscript.

ACS was developed under NASA contract NAS 5-32865, and this research has been supported by NASA grant NAG5-7697 and by an equipment grant from Sun Microsystems, Inc. The Space Telescope Science Institute is operated by AURA Inc., under NASA contract NAS5-26555. We are grateful to K. Anderson, J. McCann, S. Busching, A. Framarini, S. Barkhouser, and T. Allen for their invaluable contributions to the ACS project at JHU.

REFERENCES

- Adelberger, K. L., Steidel, C. C., Giavalisco, M., et al. 1998, *ApJ*, 505, 18
- Barthel, P. 1989, *Scientific American*, 260, 20
- Benítez, N. 2000, *ApJ*, 536, 571
- Benítez, N., Ford, H., Bouwens, R., et al. 2004, *ApJS*, 150, 1
- Bertin, E. & Arnouts, S. 1996, *A&AS*, 117, 393
- Best, P. N., Longair, M. S., & Roettgering, H. J. A. 1998, *MNRAS*, 295, 549

- Bicknell, G. V., Sutherland, R. S., van Breugel, W. J. M., et al. 2000, *ApJ*, 540, 678
- Blakeslee, J. P., Anderson, K. R., Meurer, G. R., Benítez, N., & Magee, D. 2003a, in *ASP Conf. Ser. 295: Astronomical Data Analysis Software and Systems XII*, 257
- Blakeslee, J. P., Franx, M., Postman, M., et al. 2003b, *ApJ*, 596, L143
- Bouwens, R. J., Illingworth, G. D., Blakeslee, J. P., Broadhurst, T. J., & Franx, M. 2004a, *ApJ*, 611, L1
- Bouwens, R. J., Illingworth, G. D., Blakeslee, J. P., & Franx, M. 2005a, Submitted to *ApJ*
- Bouwens, R. J., Illingworth, G. D., Broadhurst, T. J., et al. 2005b, Submitted to *ApJ*
- Bouwens, R. J., Illingworth, G. D., Thompson, R. I., et al. 2004b, *ApJ*, 606, L25
- Bruzual, G. & Charlot, S. 2003, *MNRAS*, 344, 1000
- Calzetti, D., Armus, L., Bohlin, R. C., et al. 2000, *ApJ*, 533, 682
- Charlot, S. & Fall, S. M. 1993, *ApJ*, 415, 580
- Coleman, G. D., Wu, C.-C., & Weedman, D. W. 1980, *ApJS*, 43, 393
- De Breuck, C., van Breugel, W., Röttgering, H. J. A., & Miley, G. 2000, *A&AS*, 143, 303
- De Breuck, C., van Breugel, W., Stanford, S. A., et al. 2002, *AJ*, 123, 637
- Dey, A., van Breugel, W., Vacca, W. D., & Antonucci, R. 1997, *ApJ*, 490, 698
- Djorgovski, S. G., Odewahn, S. C., Gal, R. R., Brunner, R. J., & de Carvalho, R. R. 1999, in *Astronomical Society of the Pacific Conference Series*, 179
- Djorgovski, S. G., Stern, D., Mahabal, A. A., & Brunner, R. 2003, *ApJ*, 596, 67
- Ellis, R., Santos, M. R., Kneib, J., & Kuijken, K. 2001, *ApJ*, 560, L119
- Fan, X., Strauss, M. A., Schneider, D. P., et al. 2003, *AJ*, 125, 1649
- Ferguson, H. C., Dickinson, M., Giavalisco, M., et al. 2004, *ApJ*, 600, L107
- Ferrarese, L. & Merritt, D. 2000, *ApJ*, 539, L9
- Ford, H. C., Bartko, F., Bely, P. Y., et al. 1998, in *Proc. SPIE Vol. 3356*, p. 234-248, *Space Telescopes and Instruments V*, Pierre Y. Bely; James B. Breckinridge; Eds., 234–248

- Francis, P. J., Williger, G. M., Collins, N. R., et al. 2001, *ApJ*, 554, 1001
- Gebhardt, K., Bender, R., Bower, G., et al. 2000, *ApJ*, 539, L13
- Gehrels, N. 1986, *ApJ*, 303, 336
- Giavalisco, M. & Dickinson, M. 2001, *ApJ*, 550, 177
- Giavalisco, M., Dickinson, M., Ferguson, H. C., et al. 2004a, *ApJ*, 600, L103
- Giavalisco, M., Ferguson, H. C., Koekemoer, A. M., et al. 2004b, *ApJ*, 600, L93
- Giavalisco, M., Steidel, C. C., Adelberger, K. L., et al. 1998, *ApJ*, 503, 543
- Hamana, T., Ouchi, M., Shimasaku, K., Kayo, I., & Suto, Y. 2004, *MNRAS*, 347, 813
- Heckman, T. M., Armus, L., & Miley, G. K. 1990, *ApJS*, 74, 833
- Holden, B. P., van der Wel, A., Franx, M., et al. 2005, *ApJ*, 620, L83
- Kaiser, N. 1984, *ApJ*, 284, L9
- Keel, W. C., Cohen, S. H., Windhorst, R. A., & Waddington, I. 1999, *AJ*, 118, 2547
- Kinney, A. L., Calzetti, D., Bohlin, R. C., et al. 1996, *ApJ*, 467, 38
- Klamer, I. J., Ekers, R. D., Sadler, E. M., et al. 2005, *ApJ*, 621, L1
- Kron, R. G. 1980, *ApJS*, 43, 305
- Kurk, J., Röttgering, H., Pentericci, L., Miley, G., & Overzier, R. 2003, *New Astronomy Review*, 47, 339
- Lehnert, M. D. & Bremer, M. 2003, *ApJ*, 593, 630
- Leitherer, C., Schaerer, D., Goldader, J. D., et al. 1999, *ApJS*, 123, 3
- Möller, P. & Fynbo, J. U. 2001, *A&A*, 372, L57
- Madau, P. 1995, *ApJ*, 441, 18
- Madau, P., Ferguson, H. C., Dickinson, M. E., et al. 1996, *MNRAS*, 283, 1388
- Madau, P., Pozzetti, L., & Dickinson, M. 1998, *ApJ*, 498, 106
- Magorrian, J., Tremaine, S., Richstone, D., et al. 1998, *AJ*, 115, 2285

- Miley, G. K., Overzier, R. A., Tsvetanov, Z. I., et al. 2004, *Nature*, 427, 47
- Mullis, C. R., Rosati, P., Lamer, G., et al. 2005, *ApJ*, 623, L85
- Neufeld, D. A. 1991, *ApJ*, 370, L85
- Oke, J. B. 1971, *ApJ*, 170, 193
- Ouchi, M., Shimasaku, K., Akiyama, M., et al. 2005, *ApJ*, 620, L1
- Ouchi, M., Shimasaku, K., Okamura, S., et al. 2004a, *ApJ*, 611, 660
- . 2004b, *ApJ*, 611, 685
- Papovich, C., Dickinson, M., & Ferguson, H. C. 2001, *ApJ*, 559, 620
- Papovich, C., Dickinson, M., Ferguson, H. C., et al. 2004, *ApJ*, 600, L111
- Pascarella, S. M., Windhorst, R. A., Driver, S. P., Ostrander, E. J., & Keel, W. C. 1996, *ApJ*, 456, L21
- Pentericci, L., Kurk, J. D., Röttgering, H. J. A., et al. 2000, *A&A*, 361, L25
- Pentericci, L., McCarthy, P. J., Röttgering, H. J. A., et al. 2001, *ApJS*, 135, 63
- Porciani, C. & Giavalisco, M. 2002, *ApJ*, 565, 24
- Postman, M., ACS IDT, ACS IDT, et al. 2005, *ApJ*, Accepted for publication
- Rawlings, S., Lacy, M., Blundell, K. M., et al. 1996, *Nature*, 383, 502
- Rees, M. J. 1989, *MNRAS*, 239, 1P
- Reuland, M., van Breugel, W., Röttgering, H., et al. 2003, *ApJ*, 592, 755
- Sánchez, S. F. & González-Serrano, J. I. 2002, *A&A*, 396, 773
- Schlegel, D. J., Finkbeiner, D. P., & Davis, M. 1998, *ApJ*, 500, 525
- Shapley, A. E., Steidel, C. C., Pettini, M., & Adelberger, K. L. 2003, *ApJ*, 588, 65
- Sheth, R. K. & Tormen, G. 1999, *MNRAS*, 308, 119
- Shimasaku, K., Ouchi, M., Okamura, S., et al. 2003, *ApJ*, 586, L111
- Sirianni, M., Jee, M., Benítez, N., et al. 2005, Submitted to *PASP*

- Somerville, R. S., Lee, K., Ferguson, H. C., et al. 2004, *ApJ*, 600, L171
- Speigel, D. N., Verde, L., Peiris, H. V., et al. 2003, *ApJS*, 148, 175
- Springel, V., White, S. D. M., Jenkins, A., et al. 2005, *Nature*, 435, 629
- Stanford, S. A., Eisenhardt, P. R., & Dickinson, M. 1998, *ApJ*, 492, 461
- Steidel, C. C., Adelberger, K. L., Dickinson, M., et al. 1998, *ApJ*, 492, 428
- Steidel, C. C., Adelberger, K. L., Giavalisco, M., Dickinson, M., & Pettini, M. 1999, *ApJ*, 519, 1
- Steidel, C. C., Adelberger, K. L., Shapley, A. E., Erb, D. K. and Reddy, N. A., & Pettini, M. 2005, *ApJ in Press* (astro-ph/0502432), 626, 44
- Steidel, C. C., Adelberger, K. L., Shapley, A. E., et al. 2000, *ApJ*, 532, 170
- van Breugel, W., De Breuck, C., Stanford, S. A., et al. 1999, *ApJ*, 518, L61
- Venemans, B. P., Kurk, J. D., Miley, G. K., et al. 2002, *ApJ*, 569, L11
- Venemans, B. P., Röttgering, H. J. A., Miley, G. K., et al. 2005, *A&A*, 431, 793
- Venemans, B. P., Röttgering, H., Overzier, R., et al. 2004, *A&A*, 424, L17
- Wang, J. X., Rhoads, J. E., Malhotra, S., et al. 2004, *ApJ*, 608, L21
- Wuyts, S., van Dokkum, P. G., Kelson, D. D., Franx, M., & Illingworth, G. D. 2004, *ApJ*, 605, 677
- Zirm, A., Overzier, R., Miley, G., et al. 2005, *ApJ*, 630, In press
- Zirm, A. W., Dickinson, M., & Dey, A. 2003, *ApJ*, 585, 90

Table 1. Observational Data

Field	Filter	T_{exp} (s)	A (mag)	Zeropoint (mag)	Area (arcmin ²)
TN J0924–2201	V_{606}	9400	0.167	36.4262 ^a	11.7
TN J0924–2201	i_{775}	11800	0.115	35.8202 ^a	11.7
TN J0924–2201	z_{850}	11800	0.080	35.0228 ^a	11.7
GOODS CDF-S	V_{606}	5120	0.023	26.4934 ^b	156
GOODS CDF-S	i_{775}	5120	0.017	25.6405 ^b	156
GOODS CDF-S	z_{850}	10520	0.012	24.8432 ^b	156
GOODS HDF-N	V_{606}	5000	0.035	26.4934 ^b	158
GOODS HDF-N	i_{775}	5000	0.024	25.6405 ^b	158
GOODS HDF-N	z_{850}	10660	0.018	24.8432 ^b	158
UDF-PARALLEL 1	V_{606}	22300	0.023	37.3571 ^a	11.7
UDF-PARALLEL 1	i_{775}	41400	0.016	37.1970 ^a	11.7
UDF-PARALLEL 1	z_{850}	59800	0.012	36.8038 ^a	11.7
UDF-PARALLEL 2	V_{606}	20700	0.026	37.2763 ^a	11.7
UDF-PARALLEL 2	i_{775}	41400	0.018	37.1970 ^a	11.7
UDF-PARALLEL 2	z_{850}	62100	0.013	36.8448 ^a	11.7

^aZeropoint for the total exposure (Sirianni et al. 2005).

^bZeropoint for a 1 s exposure (Giavalisco et al. 2004b).

Table 2. Properties of the spectroscopically confirmed Ly α emitters.

ID ^a	α_{J2000}	δ_{J2000}	$V_{606-i775}^b$	$i775-z850^b$	z_{850}^c	z_{spec}^d	$r_{hl,i}^e$	$r_{hl,z}^f$	SFR ^g
RG ^h	09:24:19.89	-22:01:41.23	> 2.73	0.40 \pm 0.13	25.45 \pm 0.12	5.199	0.19''	0.23''	13.8 ^{+2.2} _{-1.9}
2881 ⁱ	09:24:23.87	-22:03:43.97	2.48 \pm 0.29	0.37 \pm 0.09	25.80 \pm 0.09	5.168	0.09''	0.11''	9.7 ^{+0.6} _{-0.6}
1388 ⁱ	09:24:16.66	-22:01:16.41	2.20 \pm 0.36	0.08 \pm 0.17	26.33 \pm 0.17	5.177	0.12''	0.15''	5.9 ^{+0.8} _{-0.6}
2849 ⁱ	09:24:24.29	-22:02:30.11	> 1.85	-0.27 \pm 0.43	27.06 \pm 0.25	5.177	0.13''	0.16''	3.0 ^{+0.8} _{-0.6}
2688 ⁱ	09:24:25.65	-22:03:00.27	1.16 \pm 0.42	< -0.49	> 28.35	5.173	0.08''	–	< 1

^aIDs are from Venemans et al. (2005).

^bIsophotal color, using 2σ limits in V_{606} .

^cKron magnitude.

^dSpectroscopic redshifts from Venemans et al. (2005).

^eHalf-light radius measured in $i775$.

^fHalf-light radius measured in z_{850} .

^gSFR measured in z_{850} in $M_{\odot} \text{ yr}^{-1}$.

^hDetection based on the z_{850} image.

ⁱDetection based on the $i775$ image.

Table 3. Properties of V_{606} -dropouts in the field of TN J0924–2201.

ID	α_{J2000}	δ_{J2000}	$V_{606-i775}^b$	$i775-z850^b$	z_{850}^c	$r_{hl,z}^d$	SFR ^e	z_B^f
1873	09:24:15.17	-22:01:53.2	2.05 \pm 0.09	0.37 \pm 0.04	24.21 \pm 0.04	0''18	42	5.19 ^{+0.73} _{-0.73}
119	09:24:29.06	-22:02:41.1	1.79 \pm 0.12	0.08 \pm 0.07	24.82 \pm 0.09	0''24	24	4.74 ^{+0.68} _{-0.68}
303	09:24:29.03	-22:01:53.2	2.04 \pm 0.13	0.23 \pm 0.06	24.82 \pm 0.07	0''22	24	4.86 ^{+0.69} _{-0.69}
444	09:24:28.11	-22:01:47.4	2.35 \pm 0.32	0.16 \pm 0.12	25.20 \pm 0.11	0''28	17	4.93 ^{+0.70} _{-0.70}
1814	09:24:19.78	-22:59:58.1	> 2.18	1.07 \pm 0.15	25.29 \pm 0.09	0''24	16	5.56 ^{+0.77} _{-0.77}
310	09:24:28.10	-22:02:18.1	1.93 \pm 0.18	0.47 \pm 0.08	25.42 \pm 0.08	0''11	14	5.23 ^{+0.73} _{-0.73}
1396 (RG) ^a	09:24:19.91	-22:01:41.7	> 2.73	0.40 \pm 0.13	25.45 \pm 0.12	0''23	13	5.16 ^{+0.72} _{-0.72}
1979	09:24:12.50	-22:02:45.5	2.09 \pm 0.19	0.09 \pm 0.09	25.46 \pm 0.12	0''14	13	4.90 ^{+0.69} _{-0.69}
1802	09:24:14.92	-22:02:15.8	2.41 \pm 0.26	0.29 \pm 0.09	25.46 \pm 0.10	0''15	13	5.01 ^{+0.71} _{-0.71}
871	09:24:25.76	-22:01:11.4	2.03 \pm 0.41	0.79 \pm 0.14	25.50 \pm 0.13	0''23	13	5.39 ^{+0.75} _{-3.90}
595	09:24:27.00	-22:01:37.6	> 2.55	0.48 \pm 0.14	25.53 \pm 0.14	0''23	12	5.21 ^{+0.73} _{-0.73}
894	09:24:23.15	-22:02:16.6	2.27 \pm 0.20	0.15 \pm 0.08	25.53 \pm 0.09	0''15	12	4.92 ^{+0.70} _{-0.70}
1047	09:24:22.19	-22:01:59.6	1.74 \pm 0.16	-0.08 \pm 0.11	25.65 \pm 0.15	0''20	11	4.76 ^{+0.68} _{-0.68}
449 (2881) ^a	09:24:23.89	-22:03:44.4	2.48 \pm 0.29	0.37 \pm 0.09	25.80 \pm 0.09	0''11	9.7	5.13 ^{+0.72} _{-0.72}
1736	09:24:18.92	-22:00:42.2	1.84 \pm 0.18	0.19 \pm 0.11	25.92 \pm 0.12	0''11	8.6	4.77 ^{+0.68} _{-0.68}
670	09:24:25.41	-22:02:07.2	2.16 \pm 0.35	0.28 \pm 0.14	25.93 \pm 0.16	0''17	8.5	5.02 ^{+0.71} _{-0.71}
739	09:24:25.76	-22:01:43.0	2.84 \pm 0.50	0.16 \pm 0.12	26.09 \pm 0.15	0''12	7.4	4.94 ^{+0.70} _{-0.70}
1074	09:24:21.24	-22:02:21.6	1.98 \pm 0.30	-0.16 \pm 0.18	26.17 \pm 0.18	0''18	6.9	4.79 ^{+0.68} _{-0.68}
510	09:24:28.81	-22:01:12.2	> 2.02	1.21 \pm 0.18	26.27 \pm 0.12	0''09	6.2	5.62 ^{+0.78} _{-0.78}
1385	09:24:19.31	-22:02:01.8	2.10 \pm 0.43	0.48 \pm 0.17	26.30 \pm 0.15	0''15	6.1	5.18 ^{+0.73} _{-0.73}
1844 (1388) ^a	09:24:16.68	-22:01:16.8	2.20 \pm 0.36	0.08 \pm 0.16	26.33 \pm 0.17	0''15	5.9	4.87 ^{+0.69} _{-0.69}
505	09:24:25.42	-22:02:48.0	> 2.00	0.52 \pm 0.23	26.36 \pm 0.22	0''16	5.8	5.23 ^{+0.73} _{-1.18}
1898	09:24:14.17	-22:02:15.9	> 2.41	0.44 \pm 0.17	26.49 \pm 0.19	0''12	5.1	5.18 ^{+0.73} _{-0.73}

^aIDs between parentheses refer to Venemans et al. (2005) and Table 2.

^bIsophotal color, using 2σ limits in V_{606}

^cKron magnitude.

^dHalf-light radius measured in z_{850} .

^eUV star formation rate measured in z_{850} in $M_{\odot} \text{ yr}^{-1}$.

^fBayesian photometric redshift.

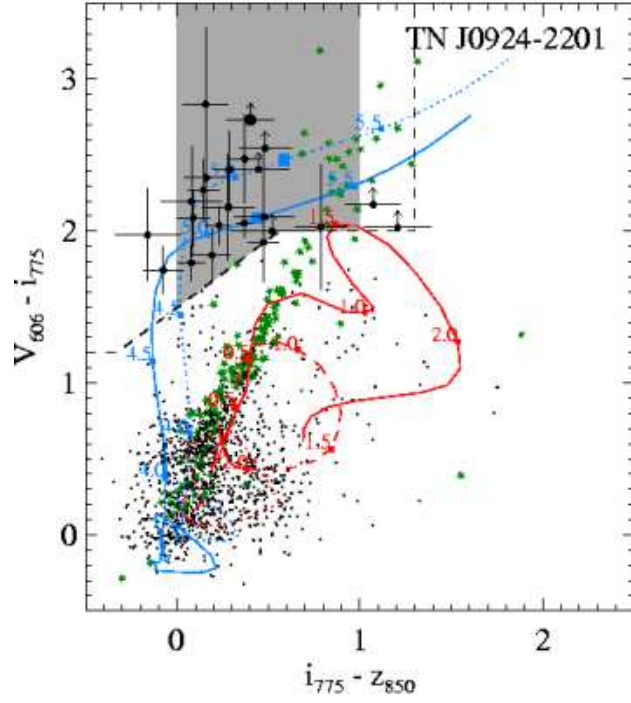


Fig. 7.— $V_{606}-i_{775}$ vs. $i_{775}-z_{850}$ color-color diagram for TN J0924–2201 candidate LBGs (solid circles) relative to objects from the full catalogue ($z_{850} < 26.5$ with $S/N > 5$). The radio galaxy is indicated by the large circle. The black dashed line is the selection window of Giavalisco et al. (2004a). The shaded region marks the selection window used for the clustering statistics of V_{606} -dropouts at $z \approx 5.2$ (see Section 4.1). The spectral tracks are from an elliptical (red solid line), a Sbc (red dashed line), a Scd (red dotted line), and a 100 Myr constant star formation model with $E(B - V) = 0.0$ (blue solid line) and $E(B - V) = 0.15$ (blue dotted line). Redshifts are indicated along the tracks. The redshift of the overdensity of Venemans et al. (2004) is marked by blue squares ($z = 5.2$). The position of the stellar locus is illustrated by the green stars (objects having $S/G > 0.85$). All colors were set to their 2σ limits (limits and error bars for field objects have been omitted for clarity).

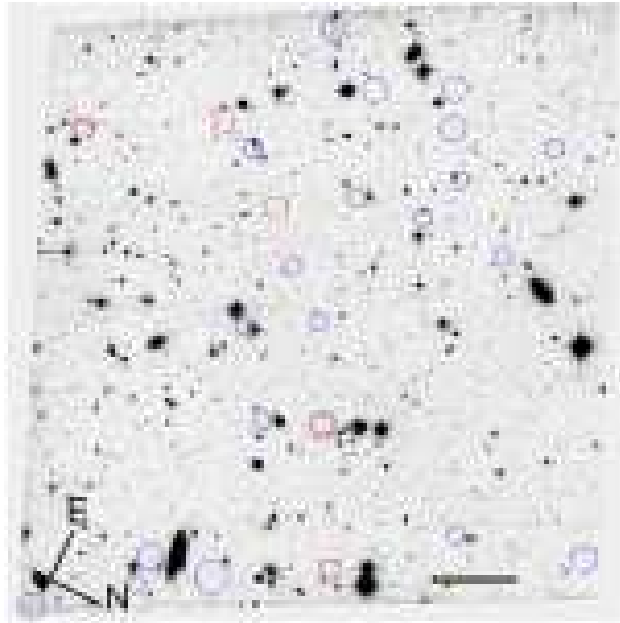


Fig. 8.— ACS z_{850} image showing the positions of the V_{606} -break objects with blue circles. The size of the circles scales with the total z_{850} magnitude of the LBGs, where the smallest circles correspond to objects with $z_{850} > 25.5$, and the largest correspond to objects brighter than $z_{850} < 24.5$. The positions of the spectroscopically confirmed $\text{Ly}\alpha$ emitters from Venemans et al. (2004) are indicated with red squares. TN J0924–2201 is located roughly $0.5'$ from the image center towards the bottom of the image (this is both a $\text{Ly}\alpha$ emitter and a V_{606} -break object). The scale bar at the bottom measures $0.5'$.

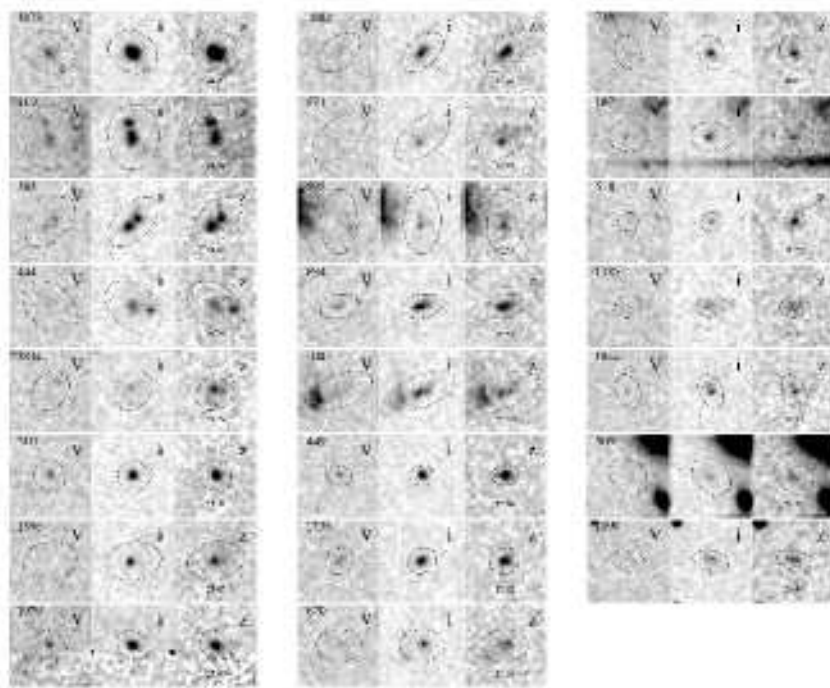


Fig. 9.— HST/ACS postage stamps showing (from left to right) V_{606} , i_{775} , and z_{850} of the $z \sim 5$ LBG sample. Each image measures $2'' \times 2''$, corresponding to $\sim 13 \times 13$ kpc at $z \sim 5$. The Kron aperture defined by the light distribution in z_{850} has been indicated. The images have been smoothed using a Gaussian kernel of $0.075''$ (FWHM).

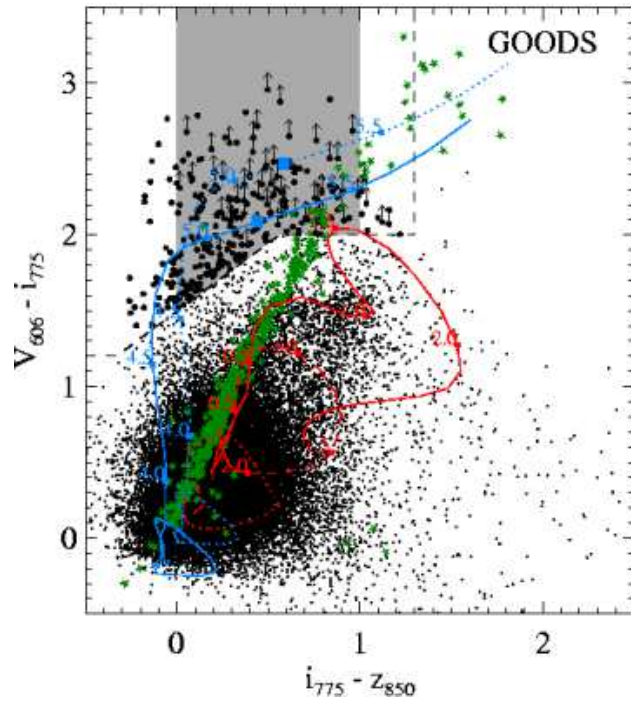


Fig. 10.— Color-color diagram of GOODS. See the caption of Fig. 7 for details.

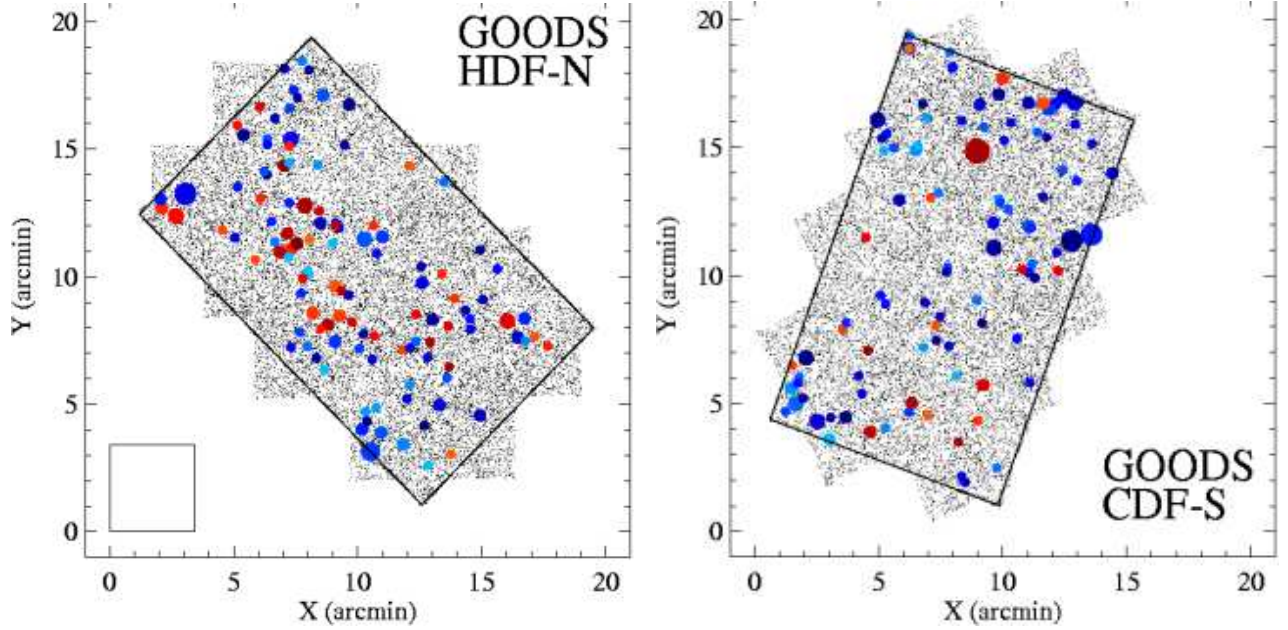


Fig. 11.— Angular distribution of V_{606} -break objects (solid circles) in the GOODS HDF-N field (left panel) and the CDF-S field (right panel), compared to the photometric sample as a whole (points). The V_{606} -dropouts have been color-coded corresponding to their $i_{775}-z_{850}$ colors (dark blue corresponds to $i_{775}-z_{850} \approx 0.0$, dark red corresponds to $i_{775}-z_{850} \approx 1.0$), which can be taken as a rough measure for the relative redshifts. The size of the symbols scales with z_{850} magnitude (the smallest symbols correspond to $z_{850} > 26.0$, the largest symbols to $z_{850} < 24.0$). The total area of the GOODS fields is $\sim 314 \text{ arcmin}^2$ (area within the solid lines). The size of a single 3.4×3.4 ACS pointing as obtained for TN J0924–2201 has been indicated to the left of the GOODS HDF-N field for comparison.

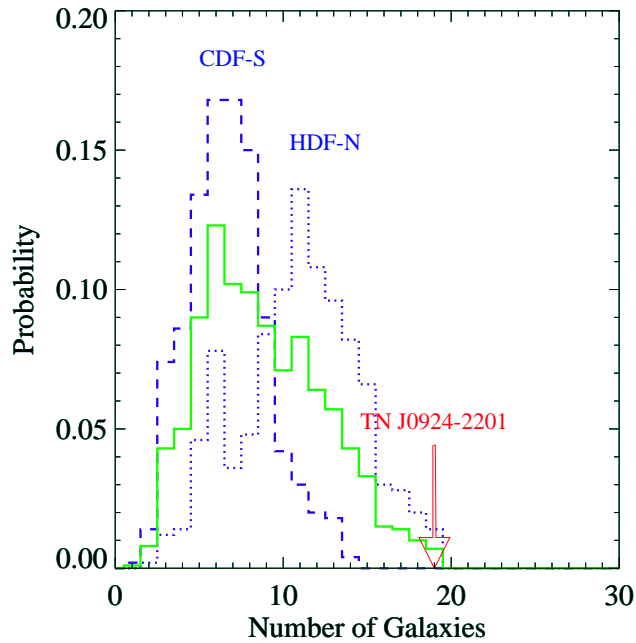


Fig. 12.— Histogram of counts-in-cells for the GOODS fields. The number of V_{606} -break objects were counted in 500 randomly placed, square cells of 11.7 arcmin² in both the CDF-S (dashed line) and the HDF-N (dotted line). The sum of the GOODS histograms is indicated (solid line). The total probability that one finds 19 objects in a single pointing in GOODS amounts to $\sim 1\%$. The number of V_{606} -break objects detected in the TN J0924–2201 field (red arrow) is anomalously high compared to GOODS. This is evidence for a population of V_{606} -dropouts associated with the radio galaxy and the Ly α emitters of Venemans et al. (2004).

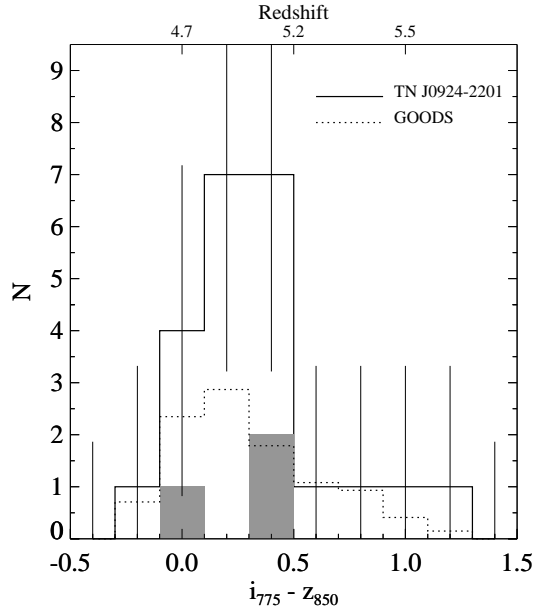


Fig. 13.— $i_{775}-z_{850}$ color distribution of the TN J0924–2201 sample (solid curve). The GOODS color distribution, normalised to the area of the TN J0924–2201 field, is shown for comparison (dotted curve). The error bars are Poissonian in the low counts regime (Gehrels 1986). The $i_{775}-z_{850}$ color of the radio galaxy and the two $\text{Ly}\alpha$ emitters that are included in the TN J0924–2201 sample are indicated by the shaded regions. The overdensity in the TN J0924–2201 field is most prominent at $0.0 < i_{775}-z_{850} < 0.5$. A slight excess in the number counts is seen around $i_{775}-z_{850} \approx 0.5$, which corresponds to $z \approx 5.2$ (see top axis) for typical values of β (i.e., -1.5 to -2).

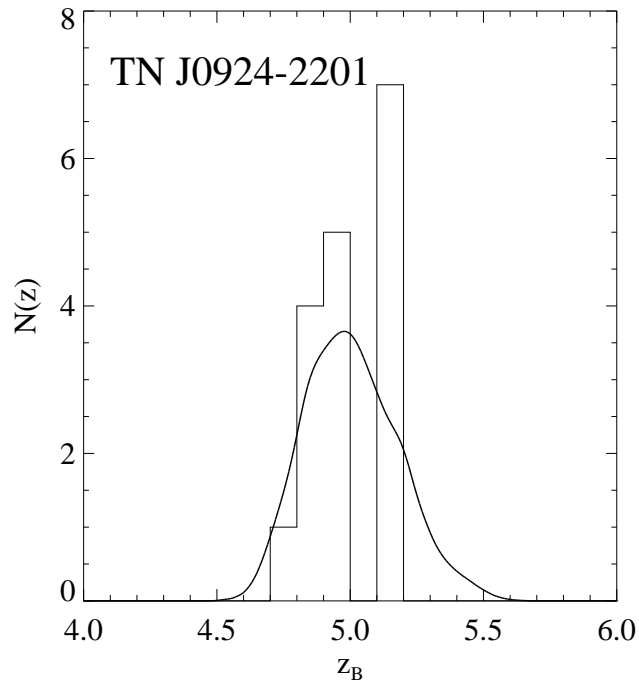


Fig. 14.— Bayesian photometric redshift histogram for V_{606} -dropouts in TN J0924-2201 having $0.0 < i_{775} - z_{850} < 1.0$ and $\text{ODDS} > 0.95$. BPZ was used with the standard redshift prior that is based on the magnitudes of galaxies in the HDF-N (see Benítez et al. 2004). The total z_B probability distribution (thick solid curve) has also been indicated.

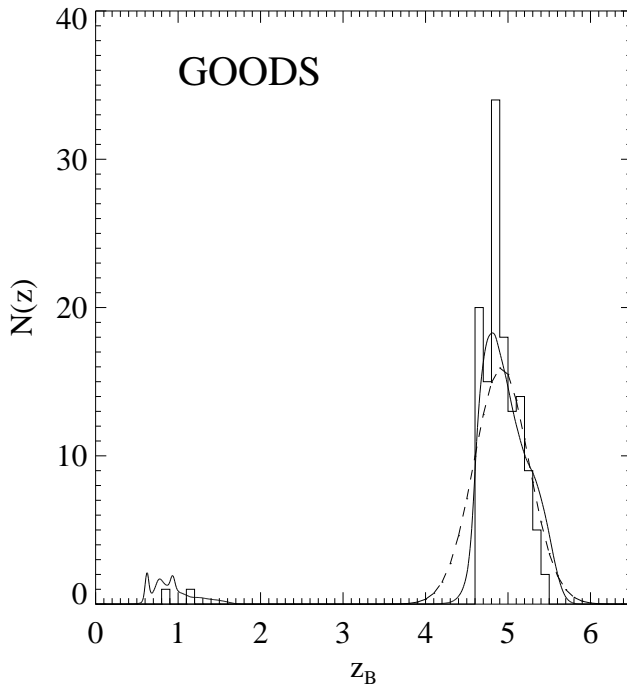


Fig. 15.— Photometric redshift histogram for the GOODS sample. Although the sample was selected using only the $V_{606}i_{775}z_{850}$ passbands, redshifts were calculated using the full $B_{435}V_{606}i_{775}z_{850}$ catalogue. The total z_B probability distribution (thick solid curve) suggests a low redshift contamination of $\sim 9\%$. The redshift distribution of Giavalisco et al. (2004a) has been indicated for comparison (dashed curve). Our distribution is narrower because of the additional constraints on $i_{775}-z_{850}$ (Eq. 3).